Published for SISSA by Springer

Received: March 22, 2023
Revised: September 14, 2023
Accepted: October 30, 2023
Published: December 4, 2023

Probing electroweak phase transition in the singlet Standard Model via $bb\gamma\gamma$ and $4l$ channels

Wenxing Zhang,[a,*] Hao-Lin Li,[b,*] Kun Liu,[a,*] Michael J. Ramsey-Musolf,[a,c,*] Yonghao Zeng[a,*] and Suntharan Arunasalam[a,*]

[a] *Tsung-Dao Lee Institute and School of Physics and Astronomy, Shanghai Jiao Tong University, 800 Dongchuan Road, Shanghai 200240, China*

[b] *Centre for Cosmology, Particle Physics and Phenomenology (CP3), Universite Catholique de Louvain, Pl. de l'Université 1, 1348 Ottignies-Louvain-la-Neuve, Belgium*

[c] *Amherst Center for Fundamental Interactions, Department of Physics, University of Massachusetts, Amherst, MA 01003, U.S.A.*

E-mail: zhangwenxing@sjtu.edu.cn, haolin.li@uclouvain.be, kun.lin@sjtu.edu.cn, mjrm@sjtu.edu.cn, zyh1678783412@sjtu.edu.cn, suntharan@sjtu.edu.cn

Abstract: We investigate the prospects for resonant di-Higgs and heavy Higgs production searches at the 14 TeV HL-LHC in the combination of $bb\gamma\gamma$ and $4l$ channels, as a probe of a possible first order electroweak phase transition in real singlet scalar extension of the Standard Model. Event selection follows those utilized in the $bb\gamma\gamma$ and $4l$ searches by the ATLAS Collaboration, applied to simulation using benchmark parameters that realize a strong first order electroweak phase transition. The output of discriminant analysis is implemented by numerical calculation, optimised by the joint restriction from the two channels. The prospective reach for $bb\gamma\gamma/4l$ channel could be more competitive in probing the electroweak phase transition at lower/higher resonance masses. With 3 ab^{-1} integrated luminosity, the combination of the $bb\gamma\gamma$ and $4l$ channels can discover/exclude a significant portion of the viable parameter space that realizes a strong first order phase transition when the resonance mass is heavier than 500 GeV.

Keywords: Specific BSM Phenomenology, Multi-Higgs Models, Higgs Properties, Other Weak Scale BSM Models

ArXiv ePrint: 2303.03612

*Corresponding author.

https://doi.org/10.1007/JHEP12(2023)018

JHEP12(2023)018

Contents

1 Introduction

As the last piece of the Standard Model(SM), the Higgs boson was discovered in 2012 at the Large Hardron Collider(LHC) [1, 2]. The SM has achieved great success in describing a plethora of electroweak and strong interaction phenomena. However, the SM fails to explain a number of observable facts about the universe. Among these is the origin of the cosmic baryon asymmetry $Y_B = n_b/s$, whose present value is $Y_B = (8.59 \pm 0.11) \times 10^{-11}$ according to the PLANCK measurement [3]. This open puzzle provides one of the strong motivations to chase after a theory of physics beyond the SM.

One of the most well-studied and experimentally testable baryogenesis scenarios is electroweak baryogenesis (EWBG) [4–7], wherein Y_B is generated in conjunction with electroweak symmetry breaking (EWSB). For a review and references, see ref. [8]. As with other baryogenesis scenarios, successful EWBG must satisfy the three "Sakharov criteria" [9, 10]: (1) baryon number violation; (2) C and CP-violation; and (3) departure from thermal equilibrium. The first two conditions guarantee that the net baryon number generation is possible. The last one is to ensure the net baryon number not be "washed out" by sphaleron process [11]. In EWBG, (3) is satisfied by the occurrence of a strong first order electroweak phase transition (SFOEWPT), which provides the conditions under which new CP-violating interactions generate the asymmetry. Within the SM, given the known mass of Higgs boson, the phase transition is a smooth crossover [10, 12]. To explain the magnitude

JHEP12(2023)018

of Y_B, new physics, especially those including new scalars coupling to the SM Higgs field, is essential to lead to a strong SFOEWPT. Based on general considerations, the presence of a first order EWPT implies that these particles must be lighter than $\sim 800 - 1000\,\text{GeV}$ and couple with sufficient strength to the Higgs boson, making them and their interactions a clear target for high energy collider studies [13].

The simplest realization of a SFOEWPT is achieved through adding one real singlet scalar in Higgs sector [14–17], which is called the real singlet-extended standard model (xSM). The scenario admits two pathways of EWSB: (i) a direct transition to the electroweak broken vacuum ("Higgs phase"), and (ii) a two-step first-order transition with the singlet scalar acquiring a vacuum expectation value (vev) before electroweak symmetry breaking. In either case, the singlet scalar may also obtain a vev in the Higgs phase. In the presence of a non-vanishing singlet vev, the singlet-like mass eigenstate and the SM-like mass eigenstate mix with each other after EWSB. Therefore, the LHC experiments searching for heavy scalar resonance shed light on exploring the viable parameter space for EWPT in the xSM [13]. Such experiments can be classified into several categories: (i) Di-Higgs channels with final states including $4b$ [18, 19], $bbVV^*$ [20–22], $bbl\nu\bar{l}\bar{\nu}$ [21], WW^*WW^* [23], bb$\tau\tau$ [24, 25] and $bb\gamma\gamma$ [26, 27]. (ii) Di-boson channels with semileptonic final states [28, 29], hadronic final states [30, 31] and leptonic final states [22, 32, 33]. (iii) Di-fermion channels [34]. On the other hand, studies have been performed for the parameter space that can realise the SFOEWPT. Heavy resonance mass up to 500 GeV can be observed by $bb\gamma\gamma$ and 4τ searches at the 14 TeV HL-LHC with lumiosity equal to 3 ab^{-1} [16]. Also, in search for signals with $bbWW^*$ final state, the singlet-like scalar mass can reach 350 GeV at the 13 TeV, 3 ab^{-1} LHC [35]. For recent study in xSM, see in refs. [16, 36–57].

Importantly, the singlet-like scalar will decay to conventional SM-like Higgs decay products due to singlet-doublet mixing as well as to di-Higgs final states (if sufficiently heavy). Thus, it is natural to ask how the combination of such "heavy Higgs" searches and resonant di-Higgs searches can further probe the SFOEWPT-viability in the xSM. In this paper, we focus on the HL-LHC collider experimental tests on the xSM, including the $pp \to h_2 \to h_1 h_1 \to bb\gamma\gamma$ and $pp \to h_2 \to ZZ \to 4\ell$ final states. Our strategy in doing so is as follows. We perform a parameter scan by requiring parameters to satisfy the theoretical bounds, including perturbativity and stability of the potential, and fix the mass and vev of SM Higgs doublet to the observed values. From the scanned parameter points, we further restrict the doublet-singlet mixing angle θ by considering the current global Higgs searches and constraints from electroweak precision observables (EWPO).[1] We select benchmark points that produce maximum and minimum $bb\gamma\gamma$ cross-section with resonance mass ranging from 260 GeV to 800 GeV and can simultaneously produce the SFOEWPT in the early universe. To analyze the perspective sensitivity of HL-LHC on testing these benchmark points, we perform collider simulations of the two aforementioned processes by following ATLAS analysis [26, 28] and obtain the signal efficiencies and distributions,

[1]A recent measurement of the W boson mass by the CDF-II collaboration deviates significantly the previous world average, which leads to difficulties in combining the measurement with previous results. Thus, in this work we will use the constraints from the fit of EWPO without including the newly measured W mass.

while The background distributions are simply rescaled from the result in the experimental paper [26, 28].

As a preview, we summarise the main result in this paper:

- For resonance mass $\gtrsim 350\,\text{GeV}$, the 4ℓ channel demonstrates much stronger detection capabilities compared with the $bb\gamma\gamma$ channel. For resonance mass $\gtrsim 600\,\text{GeV}$, this channel covers the whole viable SFOEWPT parameter space in the xSM by 5σ.
- For resonance mass $\lesssim 350\,\text{GeV}$, the $bb\gamma\gamma$ channel is relatively more powerful. The 95% C.L. upper limit for the heavy resonance mass reaches 330 GeV and 480 GeV for parameter space with minimum and maximum $bb\gamma\gamma$ cross section respectively.
- For the combined searches of the 4ℓ and $bb\gamma\gamma$ final states, if the resonance mass is located between 300 to 750 GeV, it is possible to observe or exclude the xSM SFOEWP-viable parameter space. Moreover, the 95% C.L. and 5σ upper limit lines cover the whole viable parameter space for the resonance mass $\gtrsim 550\,\text{GeV}$ and $\gtrsim 600\,\text{GeV}$ respectively.
- A strong correlation between the signs of the mixing angle θ and the heavy Higgs to SM-like Higgs coupling g_{211} is observed for SFOEWPT-viable parameter space.

Our discussion of the analysis leading to these conclusions is organized as follows: in section 2, we introduce the xSM framework and the various restrictions on the parameter space: perturbativity, global Higgs searches and EWPO. In section 3, we consider the one-loop effective potential with high-T approximation and perform a general scan over the allowed parameter space to obtain regions compatiable with a SFOEWPT. Section 4 performs a parameter scan with constraints from discribed above. Benchmark paramater choices yielding minimum and maximum $bb\gamma\gamma$ cross sections and SFOEWPT are listed in the end of this section. Section 5 performs the $bb\gamma\gamma$ and 4ℓ simulation based on 13 TeV experiments and extrapolates the result to 14 TeV 3000fb^{-1}. Section 6 presents the discrimination between signal and background events. Further it draws conclusions about the sensitivity of exclusion ability. Section 7 is dedicated to the conclusions. In the appendix, subsection A.1 details the 1-loop RGE of xSM used for analyzing the perturbativity bound. Subsections A.2 and A.3 demonstrate the details of the simulation of $bb\gamma\gamma$ and 4ℓ respectively. Subsection A.4 calculates the impact from the current CDF-II W-boson mass measurement on the heavy Higgs mass and the mixing angle.

2 The xSM model

We consider a minimal extension of SM that includes a gauge singlet real scalar S. The most general renormalizable scalar potential is given by [15]

$$V_0(H,S) = -\mu^2(H^\dagger H) + \lambda(H^\dagger H)^2 + \frac{a_1}{2}(H^\dagger H)S + \frac{a_2}{2}(H^\dagger H)S^2 + \frac{b_2}{2}S^2 + \frac{b_3}{3}S^3 + \frac{b_4}{4}S^4, \tag{2.1}$$

where H is the SM $\mathrm{SU}(2)_L$ scalar doublet. The fields H and S obtain vevs after spontaneous EWSB. They may be cast into the form

$$S = x_0 + s, \tag{2.2}$$

$$H = \begin{pmatrix} G^+ \\ \frac{1}{\sqrt{2}}(v_0 + h + iG^0) \end{pmatrix}. \tag{2.3}$$

The a_1 and a_2 terms with a non-zero VEV of the singlet introduce mixing and a portal interaction between the SM Higgs and the singlet. The absence of a_1 and b_3 leads to a Z_2 symmetry that protects the singlet from mixing with SM particles if x_0 vanishes, and hence the singlet becomes a DM candidate. However, even if the potential preserves the Z_2 symmetry explicitly, appropriate potential parameters can lead to a spontaneous Z_2 breaking, which yields a non-zero x_0 and mixes the SM Higgs and singlet scalar through the a_2 term, thereby allowing the decay of both h_1 and h_2 to SM particles. For a recent analysis of this possibility, see ref. [41]. A first order EWPT may arise in several ways [15, 58–61] (a) a one-step transition to the present Higgs phase wherein $x_0 = 0$; (b) a one-step transition to a EWSB vacuum in which the vevs of both H^0 and S are non-vanishing; (c) a two-step transition, where the vacuum in the first step has $H^0 = 0$ and $S \neq 0$ while the vacuum at the end of the second step has $H^0 \neq 0$ and $S \neq 0$. Case (a) requires thermal loop contributions from S to generate a sufficiently large barrier between the symmetric and EWSB phases. For scenario (b), the cubic portal term can induce a tree-level barrier for $a_1 < 0$. The second step of the two-step history (c) will be first order due to the cross-quartic portal term with $a_2 > 0$. In the following, we study the SFOEWPT and its di-Higgs signal phenomenology.

The minimization (tadpole) conditions in xSM potential can be utilized to trade the two potential parameters μ^2 and b_2 with vevs of the two scalars:

$$\mu^2 = \lambda v_0^2 + (a_1 + a_2 x_0)\frac{x_0}{2}, \tag{2.4}$$

$$b_2 = -b_3 x_0 - b_4 x_0^2 - \frac{a_1 v_0^2}{4x_0} - \frac{a_2 v_0^2}{2}. \tag{2.5}$$

The mass matrix of the scalar sector can be derived by taking the second derivatives of the scalar potential and evaluating their value at the scalar vevs:

$$\mathcal{M}^2 = \begin{pmatrix} m_s^2 & m_{hs}^2 \\ m_{hs}^2 & m_h^2 \end{pmatrix}. = \begin{pmatrix} -\frac{a_1 v_0^2}{4x_0} + x_0\,(b_3 + 2b_4 x_0) & \frac{v_0}{2}\,(a_1 + 2a_2 x_0) \\ \frac{v_0}{2}\,(a_1 + 2a_2 x_0) & 2\lambda v_0^2 \end{pmatrix}. \tag{2.6}$$

The above scalar mass matrix can be diagonalized by the mixing matrix parameterized by the mixing angle θ:

$$O(\theta)^T \mathcal{M}^2 O(\theta) = \begin{pmatrix} m_1 & 0 \\ 0 & m_{h_2} \end{pmatrix}, \qquad O(\theta) = \begin{pmatrix} \cos\theta & -\sin\theta \\ \sin\theta & \cos\theta \end{pmatrix}, \tag{2.7}$$

where $m_{h_1} = 125.25$ GeV [62] corresponds to the mass of SM-like mass eigenstate. h_2 is the singlet-like mass eigenstate, such that the Higgs fields can be expressed as

$$h_1 = h\cos\theta + s\sin\theta \tag{2.8}$$

$$h_2 = s\cos\theta - h\sin\theta. \tag{2.9}$$

To guarantee the stability of the potential, the coefficient of the quartic field term should be positive definite, where the quartic field term is expressed as

$$V(h,s) \supset \begin{pmatrix} h^2 & s^2 \end{pmatrix} \begin{pmatrix} \frac{\lambda}{4} & \frac{a_2}{8} \\ \frac{a_2}{8} & \frac{b_4}{4} \end{pmatrix} \begin{pmatrix} h^2 \\ s^2 \end{pmatrix}. \tag{2.10}$$

The stability condition requires $a_2 \geq -2\sqrt{\lambda b_4}$. Furthermore we need to guarantee that the local potential minimum at (v_0, x_0) is the global one, which is checked numerically by evaluating the potential at all possible extreme points.

3 Electroweak phase transition

The character of EWPT is understood in terms of the finite-T effective potential. It is well-known that in the conventional treatment, $V_{\text{eff}}^{T\neq 0}$, which is derived from the gauge-dependent 1PI effective action, suffers from gauge-dependence [37–40]. However, in the high temperature expansion, wherein the potential is expanded in powers of the temperature, the leading field- and temperature-dependent term that arises at $\mathcal{O}(T^2)$ is gauge-independent when evaluating the potential at the tree-level minimum of the fields according to the $\hbar$-expansion prescription [37]. For the same reason, the 1-loop zero-temperature Coleman-Weinberg potential, V_{CW} is also gauge independent. Therefore, in this paper, we employ the gauge-independent high-T approximated potential, which is composed of the tree-level potential, zero-temperature Coleman-Weinberg potential, V_{CW}, and the gauge-independent finite-temperature corrections expanded up to $\mathcal{O}(T^2)$.

We start by introducing the zero-temperature Coleman-Weinberg potential as follows:

$$V_{\text{CW}} = \sum_k \frac{(-1)^{2s_k}}{64\pi^2} g_k \, [M_k^2]^2 \left(\ln \frac{M_k^2}{\Lambda^2} + \frac{3}{2} \right), \tag{3.1}$$

wherein the summation contains all fields that interact with the scalar fields h and s. The s_k is the spin of the particle, and M_k is the mass. The Λ is the renormalization scale, which is fixed to be v_0.

The high-T approximation for bosonic fields and fermion fields are expressed according to [15]

$$V_{\text{High-T}}^{\text{scalar}} = \frac{g_s T^4}{2\pi^2} \left(-\frac{\pi^4}{45} + \frac{\pi^2}{12} \frac{m_k^2}{T^2} - \frac{\pi}{6} \left(\frac{(m_k^2)^{3/2}}{T^3} \right) - \frac{m_k^4}{32 T^4} \log \left(\frac{m_k^2}{c_B T^2} \right) \right) \tag{3.2}$$

$$V_{\text{High-T}}^{\text{fermion}} = -\frac{g_f T^4}{2\pi^2} \left(-\frac{7\pi^4}{360} - \frac{\pi^2}{24} \frac{m_k^2}{T^2} - \frac{m_k^4}{32 T^4} \log \left(\frac{m_k^2}{c_F T^2} \right) \right) \tag{3.3}$$

$$\tag{3.4}$$

respectively, where the $g_{s/f}$ is the number of degrees of freedom for scalars/fermions. We ignore the field-independent terms and keep the gauge-independent contributions up to the leading order of temperature. The high-T potential approximation then gives

$$V_{\text{High-T}} \simeq \frac{T^2}{24} \left(3M_g^2 + M_h^2 + M_s^2 + 6M_W^2 + 3M_Z^2 \right) + \frac{T^2}{48} \left(12 M_t^2 \right), \tag{3.5}$$

where the field-dependent Goldstone, Higgs, and scalar masses are given by

$$M_g^2 = -\mu^2 + \lambda h^2 + \frac{s}{2}(a_1 + a_2 s) \tag{3.6}$$

$$M_h^2 = M_g^2 + 2\lambda h^2 \tag{3.7}$$

$$M_s^2 = b_2 + \frac{a_2}{2}h^2 + 2b_3 s + 3b_4 s^2. \tag{3.8}$$

Note that after EWSB $M_g^2 = 0$, as can be seen from the tadpole conditions.

In the leading order of the high-T approximation, field-dependent thermal corrections appear in terms of quadratic in the scalar fields. By themselves, these thermal mass contributions do not generate a barrier between the origin and the global minima. Such a barrier can arise as follows, corresponding to the scenarios identified in section 2: (a) For the one-step direct transition to a pure Higgs phase, thermal loops, generated by the cross-quartic interaction proportional to a_2, can enhance the SM contributions to the Th^3-induced barrier; (b) for the one-step transition to the mixed vev-vacuum, the Z_2 breaking interactions proportional to a_1 and b_3 can generate a tree-level barrier, whose effect becomes active as T decreases due to the thermal mass contributions; (c) in the two-step scenario, the cross-quartic interaction proportional to a_2 generates a tree-level barrier between the pure singlet and Higgs (or mixed singlet-Higgs) vacuum; the effect of this barrier again depends on T due to the thermal mass contributions to the potential. In the present analysis, we retain only the gauge-invariant thermal mass contributions to the potential, so our parameter choices do not include the direct one-step transition (a). We defer an analysis of this case to future work.

In practice, we compute phase transition-relevant quantities using the CosmoTransitions package [63]. We obtain the critical temperature T_c at which the broken and unbroken phases are degenerate and the corresponding Higgs vev v_c. Both quantities are readily gauge invariant in the leading order high-T approximation. The condition for a strong first-order phase transition is approximately given by

$$\frac{v_c}{T_c} \gtrsim 1. \tag{3.9}$$

4 Constraints on parameters and numerical results

In this section, we discuss the details of our parameter scan and all the relevant theoretical and experimental constraints. In the xSM, the potential includes seven parameters: a_1, a_2, b_3, b_4, λ, μ^2, and b_2. By utilizing the tadpole condition described in eqs. (2.4), it is possible to trade two parameters, μ^2 and b_2, for the vacuum expectation values (vev) of scalars, denoted as v_0 and x_0. Additionally, we fix the SM Higgs vev v_0 to be 246 GeV and the mass of the SM-like Higgs m_{h_1} to be 125.25 GeV [62], which reduces the number of free parameters in the theory to five. Since the off-diagonal elements m_{hs}^2 in the mass matrix given by equation (2.6) have a simple linear relation to a_2, and m_h^2 and m_s^2 are independent of a_2, we can express a_2 in terms of the remaining parameters as

$$a_2 = \frac{\pm\sqrt{m_h^2 m_s^2 - m_{h_1}^2(m_h^2 + m_s^2 - m_{h_1}^2)} - a_1 v_0/2}{x_0 v_0}. \tag{4.1}$$

In practice, we determine whether to choose the plus or minus sign in eq. (4.1) based on whether the resulting parameter point achieves the global minimum at (v_0, x_0). If both signs satisfy the criteria, we randomly select one of the solutions. In the meantime, we also require the mass of the heavy Higgs $m_{h_2} > 2m_{h_1}$ to enable the di-Higgs decay channel.

Consequently, we have five free parameters $a_1, b_3, b_4, \lambda, x_0$ to be scanned. We limit the range of the dimensionful parameters a_1, b_3, and x_0 to be within 1 TeV, specified as:

$$-1 < \frac{a_1}{\text{TeV}}, \frac{b_3}{\text{TeV}} < 1, \quad 0 < x_0 < 1 \text{ TeV}. \tag{4.2}$$

We choose this range due to the difficulty in finding parameter space that can yield a SFOEWPT with a heavy scalar boson mass m_{h_2} exceeding 1 TeV.[2] As for x_0, we only scan the positive branch since the negative branch can be covered by reversing the signs of a_1 and b_3.

Regarding the dimensionless parameters λ and b_4, we perform a test scan with their range to be within the naive parturbativity bounds — $0 < \lambda, b_4 < 2\pi/3$ [64]. As we have assumed the renormalization scale for these parameters are defined at the electroweak symmetry breaking scale v_0 in obtaining the zero-temperature Coleman-Weinberg potential, we further check whether these dimensionless parameters after running to 10 TeV with one-loop RGEs[3] are still within their naive perturbativity bounds: $0 < 6\lambda, 6b_4, |a_2| < 4\pi$. For those around 150,000 parameter points that survive from this perturbativity requirement after running, we find that the upper limits for the scanned dimensionless parameters λ and b_4 to be 1.052 and 0.868 respectively. Therefore to increase the scanning efficiency, we decided to specify ranges for dimensionless parameters to be narrower than given by the naïve perturbativity bounds:

$$0 < \lambda, b_4 < 1. \tag{4.3}$$

We leave the details for full expressions of the renormalization group equations (RGEs) and the relevant values for input parameters in appendix A.1. During the parameter scan, we assume flat distributions for all the scanned parameters and trace the finite temperature potentials using CosmoTransitions for each obtained parameter point that satisfies the aforementioned theoretical constraints. Subsequently, we focus on selecting points that are capable of generating a SFOEWPT in the early universe. Following this selection process, we find approximately 80,000 parameter points that meet the desired criteria out of 6 million scans.

As for the experimental bounds, the first constraint we consider is from the electroweak precision observables (EWPO). In the xSM, the oblique parameters receive additional contributions that depend on the singlet-like scalar mass m_{h_2} and its mixing angle $\sin\theta$, and a constraint has been derived shows that the upper limit of $|\sin\theta|$ varies from 0.35 to 0.2 when the resonance mass satisfies 250 GeV $< m_{h_2} <$ 950 GeV [65]. However, the new measurement of m_W from CDF experiments indicates a very different parameter region from the previous measurement [66] and receives a lot of debate because of its deviation from

[2] Note that the dearth of SFOEWPT-viable parameter points for a_1 and b_3 in this regime is consistent with the general arguments of ref. [13].

[3] Running to higher scale results in stronger bounds.

the other measurements. Therefore, in what follows, we will utilize the EWPO constraints without including the new value of m_W for reasons discussed in detail in section A.4.

Secondly, we incorporate the constraints arising from the measurements of the signal strength of the Standard Model Higgs boson. The most recent results from ATLAS [67] and CMS [68] for LHC Run-2, assuming a global rescaling of the signal strength μ, are as follows:

$$\mu_{\rm ATLAS} = 1.05 \pm 0.06, \quad \mu_{\rm CMS} = 1.02^{+0.07}_{-0.06}. \tag{4.4}$$

By utilizing these measurements, we deduce that $|\sin\theta| < 0.193$ at a 95% confidence level (CL). Thus, it becomes evident that the Higgs signal strength measurement imposes a more stringent constraint than the EWPO.

Apart from the SM-like Higgs, we also study the current and future prospective collider phenomenology for the heavy singlet-like resonance production at the 14 TeV HL-LHC. Since $m_{h_2} > 2m_{h_1}$, the decay of $h_2 \to h_1 h_1$ and $h_2 \to X_{\rm SM} X_{\rm SM}$ is allowed, where the $X_{\rm SM}$ stands for SM particle whose mass is less than $m_{h_2}/2$. Since the haevy Higgs h_2 interact with the SM particles through the mixing with the SM Higgs h, the total decay width of the heavy scalar h_2 can be written as

$$\Gamma_{h_2} = \Gamma_{h_2 \to h_1 h_1} + \sin^2\theta\, \Gamma^{\rm SM}(m_{h_2}), \tag{4.5}$$

where the $\Gamma^{\rm SM}(m_{h_2})$ denotes the decay width function of standard model Higgs with a mass of m_{h_2}. The decay width of $h_2 \to h_1 h_1$ in the equation above is

$$\Gamma_{h_2 \to h_1 h_1} = \frac{g_{211}^2 \sqrt{1 - \frac{4m_{h_1}^2}{m_{h_2}^2}}}{8\pi m_{h_2}}, \tag{4.6}$$

where the tri-Higgs coupling is obtained from the tree-level potential:

$$\begin{aligned} g_{211} = \frac{1}{4}[&(a_1 + 2a_2 x_0)\cos^3\theta + 4v_0\,(a_2 - 3\lambda)\cos^2\theta\sin\theta \\ &- 2\,(a_1 + 2a_2 x_0 - 2b_3 - 6b_4 x_0)\cos\theta\sin^2\theta - 2a_2 v_0 \sin^3\theta]. \end{aligned} \tag{4.7}$$

As a result, the branching ratio for $h_2 \to h_1 h_1$ can be expressed as

$$BR(h_2 \to h_1 h_1) = \frac{\Gamma_{h_2 \to h_1 h_1}}{\Gamma_{h_2 \to h_1 h_1} + \sin^2\theta\, \Gamma^{\rm SM}(m_{h_2})}. \tag{4.8}$$

In this work, we focus on the di-Higgs channel with $bb\gamma\gamma$ final state and di-boson channel with four lepton final state. The cross-section of $pp \to h_2 \to h_1 h_1 \to bb\gamma\gamma$ and $pp \to h_2 \to VV^* \to \ell\bar{\ell}\ell\bar{\ell}$ channels are calculated with narrow width approximation expressed in the following equations,

$$\sigma_{bb\gamma\gamma} = \sigma_{pp \to h_2} \times BR(h_2 \to h_1 h_1) \times BR(h_1 \to b\bar{b}) \times BR(h_1 \to \gamma\gamma), \tag{4.9}$$

$$\sigma_{4\ell} = \sigma_{pp \to h_2} \times BR(h_2 \to ZZ) \times BR(ZZ \to 4\ell), \tag{4.10}$$

where the production cross section for heavy Higgs can be expressed as $\sigma_{pp \to h_2} = \sin^2\theta \times \sigma_H(m_{h_2})$, and $\sigma_H(m_{h_2})$ is the SM Higgs production cross section if its mass were to be m_{h_2} given by the CERN recommendation [69].

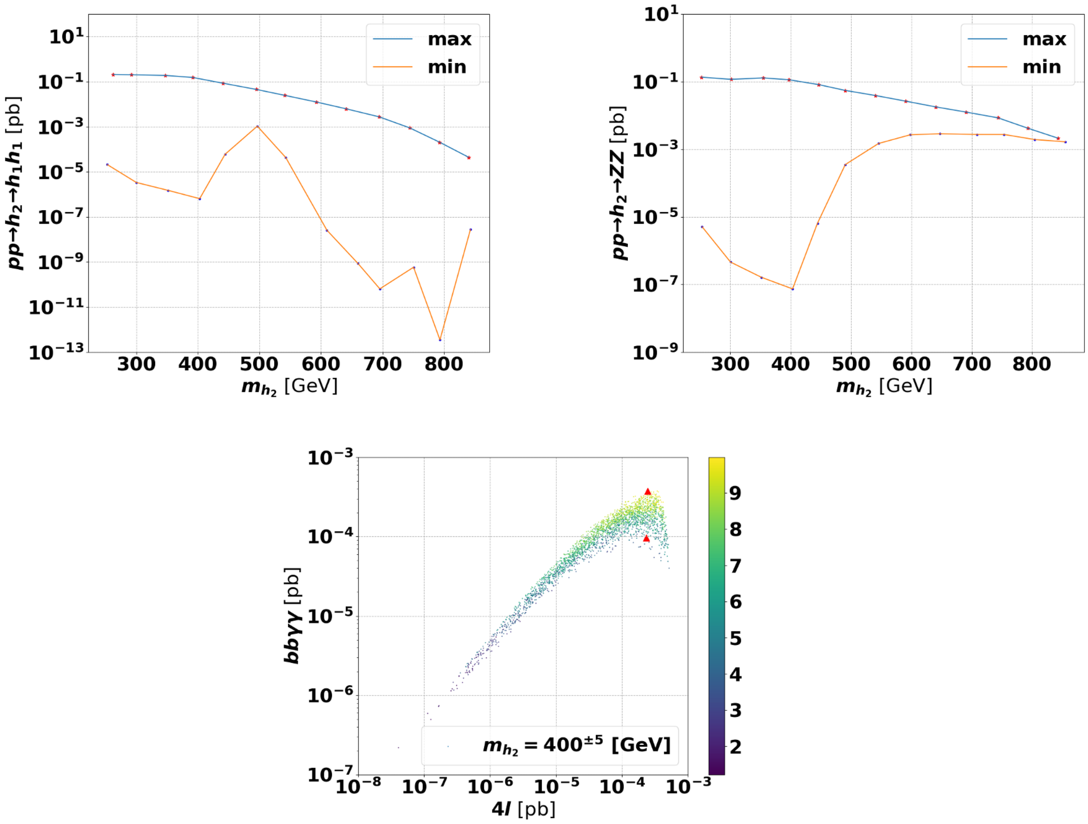

Figure 1. The maximum/minimum of the cross sections of $bb\gamma\gamma$ and 4l channels that realize SFOEWPT. The color bar stands for first-order EWPT strength. The red points in the third panel are the maximum and minimum benchmarks we choose for $m_{h_2} = 402\,\text{GeV}$ and $m_{h_2} = 401\,\text{GeV}$ in the table 1 and table 2 respectively.

To estimate the ability of the HL-LHC in investigating EWPT in the xSM, we collect all the points in the scan that realize SFOEWPT. Among these points, for a given h_2 mass, the cross sections of bb$\gamma\gamma$ and 4ℓ channels vary from their minimum to the maximum depending on the choice of other parameters. In figure 1, we show the maximum and minimum cross sections for consecutive intervals of 50 GeV starting from 250 GeV. Among selected points, benchmarks with given fixed 4ℓ cross sections that maximize/minimize bb$\gamma\gamma$ cross sections are listed in the table 1/table 2.

The scanned result is illustrated in the figure 2, where we plot the cross section for $pp \to h_2 \to h_1 h_1 \to b\bar{b}\gamma\gamma$ and $pp \to h_2 \to VV^* \to 4\ell$ to show their correlation. In the following sections, we show the key results from our simulations for the two channels and derive the prospective bounds for future HL-LHC.

5 Simulation of signal and background distributions

The strategy of signal and background simulation is as follows: two 13 TeV ATLAS analyses channels $pp \to h_2 \to h_1 h_1$ [26] and $pp \to h_2 \to VV^*$ [22] where $h_1 \to b\bar{b}/\gamma\gamma$ and $V \to \ell\bar{\ell}$, are taken as references for event selection and background distribution. A factor of 1.18

Benchmark	$\sin\theta$	g_{211}(GeV)	m_{h_2}(GeV)	a_1(GeV)	a_2	b_3(GeV)	b_4	λ	v_x(GeV)	σ_{4l} (pb)	$\sigma_{bb\gamma\gamma}$ (pb)
B1	0.181	52	262	-418	2.64	-244	0.647	0.143	78.5	$3.09{\times}10^{-4}$	$5.50{\times}10^{-4}$
B2	0.189	60	297	-435	3.23	-365	1.126	0.162	63.8	$2.89{\times}10^{-4}$	$5.27{\times}10^{-4}$
B3	0.185	74	347	-554	4.23	-361	1.411	0.210	63.2	$3.01{\times}10^{-4}$	$4.99{\times}10^{-4}$
B4	0.174	91	402	-664	5.83	-470	1.399	0.291	55.8	$2.43{\times}10^{-4}$	$3.72{\times}10^{-4}$
B5	0.167	92	445	-694	6.29	-338	1.093	0.313	50.5	$1.83{\times}10^{-4}$	$2.13{\times}10^{-4}$
B6	0.152	102	495	-766	8.16	-411	1.569	0.411	45.1	$1.04{\times}10^{-4}$	$1.159{\times}10^{-4}$
B7	0.152	105	546	-823	9.51	-523	1.856	0.501	40.0	$7.72{\times}10^{-5}$	$6.08{\times}10^{-5}$
B8	0.145	106	595	-876	10.34	-34	2.051	0.561	38.1	$5.06{\times}10^{-5}$	$3.14{\times}10^{-5}$
B9	0.137	102	646	-897	11.25	217	1.995	0.619	33.7	$3.21{\times}10^{-5}$	$1.49{\times}10^{-5}$
B10	0.150	85	696	-983	10.91	229	2.039	0.628	31.9	$3.01{\times}10^{-5}$	$6.02{\times}10^{-6}$
B11	0.142	68	748	-998	11.32	333	1.974	0.662	28.0	$1.94{\times}10^{-5}$	$2.06{\times}10^{-6}$

Table 1. Benchmark parameter choices that maximize the $bb\gamma\gamma$ channel cross section when the 4ℓ cross section is fixed.

Benchmark	$\sin\theta$	g_{211}(GeV)	m_{h_2}(GeV)	a_1(GeV)	a_2	b_3(GeV)	b_4	λ	v_x(GeV)	σ_{4l} (pb)	$\sigma_{bb\gamma\gamma}$ (pb)
B1	0.135	19	262	-187	1.52	169	0.766	0.130	50.5	$3.03{\times}10^{-4}$	$5.64{\times}10^{-5}$
B2	0.155	25	299	-232	1.78	210	0.847	0.124	46.7	$3.05{\times}10^{-4}$	$1.41{\times}10^{-4}$
B3	0.146	33	353	-291	2.65	174	1.166	0.165	38.9	$2.90{\times}10^{-4}$	$1.36{\times}10^{-4}$
B4	0.142	37	403	-349	3.11	325	0.748	0.163	36.0	$2.35{\times}10^{-4}$	$9.64{\times}10^{-5}$
B5	0.142	32	447	-373	3.39	348	1.229	0.177	30.6	$1.84{\times}10^{-4}$	$3.68{\times}10^{-5}$
B6	0.136	42	504	-467	4.68	265	0.959	0.235	29.3	$1.05{\times}10^{-4}$	$2.37{\times}10^{-5}$
B7	0.137	40	551	-528	5.04	544	1.075	0.272	28.3	$7.66{\times}10^{-5}$	$1.04\ {\times}10^{-5}$
B8	0.135	31	603	-580	5.44	644	1.525	0.272	25.8	$5.10{\times}10^{-5}$	$3.17{\times}10^{-6}$
B9	0.129	39	651	-667	7.24	424	1.926	0.358	24.8	$3.25{\times}10^{-5}$	$2.53{\times}10^{-6}$
B10	0.149	13	704	-801	6.28	561	1.384	0.354	25.8	$3.06{\times}10^{-5}$	$1.39{\times}10^{-7}$
B11	0.141	8	754	-857	6.94	927	1.655	0.393	24.2	$1.95{\times}10^{-5}$	$3.09{\times}10^{-8}$

Table 2. Benchmark parameter choices that minimize the $bb\gamma\gamma$ channel cross section when the 4l cross section is fixed.

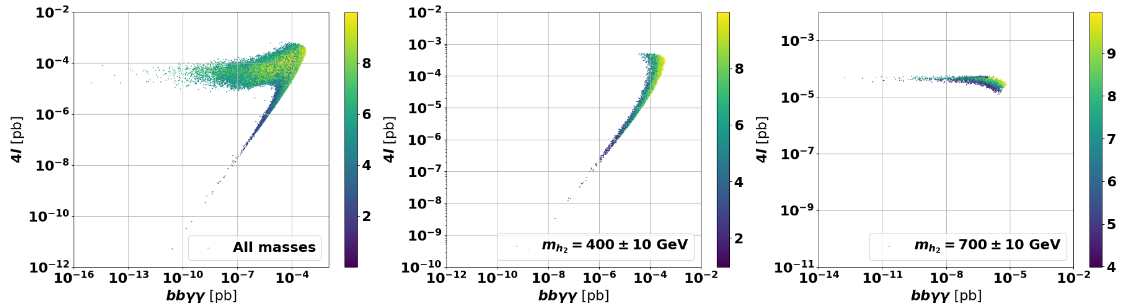

Figure 2. Distribution of the cross sections for the $bb\gamma\gamma$ and 4ℓ channels. The color stands for first-order EWPT strength as defined in eq. (3.9). The left panel shows all results with m_{h_2} varying from 260 GeV to 800 GeV. The masses in the middle and right plots are within 400 ± 10 GeV and 700 ± 10 GeV, respectively.

JHEP12(2023)018

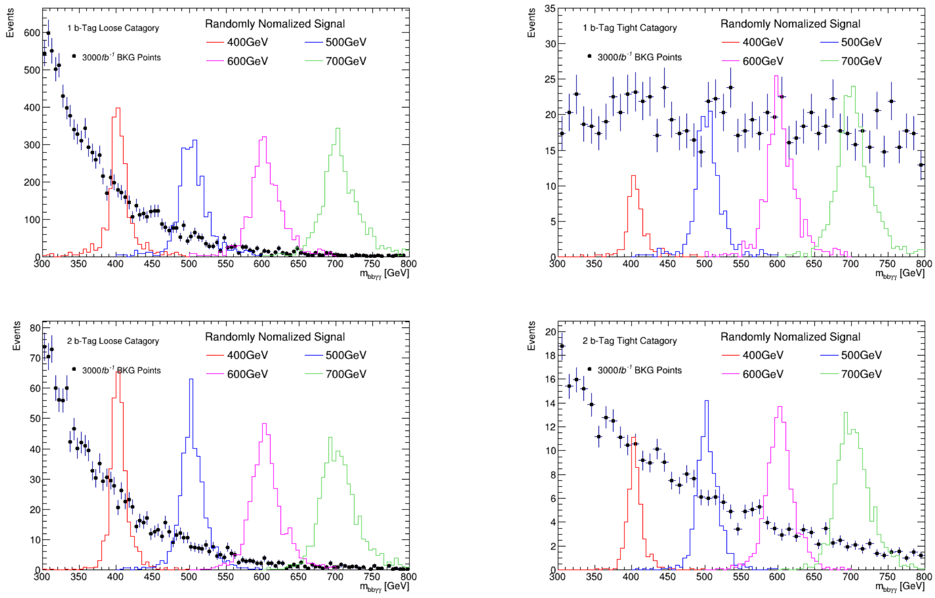

Figure 3. The $m_{bb\gamma\gamma}$ distributions of the $bb\gamma\gamma$ channel analysis, in four signal-enriched regions: "1-btag loose", "2-btag loose", "11-btag tight" and "2-btag tight", respectively. The normalization of signal processes are arbitrary.

is applied to backgrounds to count for collision energy upgrade from 13 TeV to 14 TeV, as commonly used in ATLAS prospective studies. The signal processes at 14 TeV center-of-mass energy are generated for heavy singlet-like mass states, whose mass ranges from 270 GeV to 800 GeV in steps of 50 GeV. The simulation process is presented briefly in the following, with more details of signal cut-flow being given in appendix A.

In the $bb\gamma\gamma$ channel as described in reference [26], the four-body invariant mass $m_{bb\gamma\gamma}$ is used as the discriminating variable. Events are categorized into four signal-enriched regions according to number of b-tagged jets as well as loose and tight event selection criteria: "1-btag loose", "2-btag loose", "1-btag tight" and "2-btag tight". The "1-btag" and "2-btag" means that at least one and two jets should be recognized as b-jets. Acceptances after passing signal-enriched region are in good agreement with the reference analysis, as shown in table 3 in appendix A. For background, the $m_{bb\gamma\gamma}$ distributions from reference analysis are extracted. An exponential function is used to fit the $m_{bb\gamma\gamma}$ curve in each signal-enriched region, and then use the fitted function to generate $m_{bb\gamma\gamma}$ distributions according to 3 ab^{-1} luminosity. An $\pm 2\%$ error value is assigned as luminosity calculation uncertainty. The $bb\gamma\gamma$ distributions of signal and background are shown in figure 3. The normalizations of signals on the plots are arbitrary.

In the $VV \to 4\ell$ channel, as described in the reference [22], the four-body invariant mass $m_{4\ell}$ is used as the discriminating variable. Events have to pass signal-enriched region selection, which is given with more details in appendix A section B). Signal efficiency is in reasonable agreement with the reference analysis. A similar approach as $bb\gamma\gamma$ analysis is used to simulate background distributions. Figure 4 shows the $m_{4\ell}$ distributions of signal and background processes. The normalization of signals on the plots are arbitrary.

JHEP12(2023)018

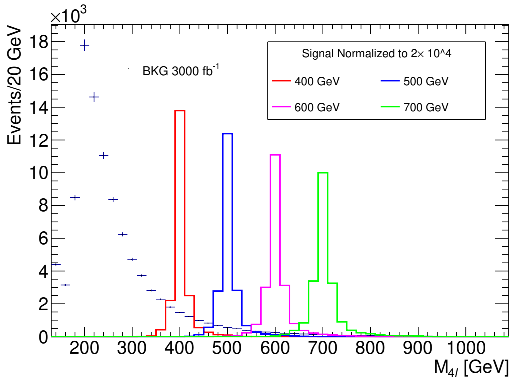

Figure 4. Distribution of reconstructed four charged leptons for $h_2 \to ZZ \to 4\ell$. The number of signal events is normalized to 2×10^4. The number of background events is normalized with the integrated luminosity of 3 ab^{-1}.

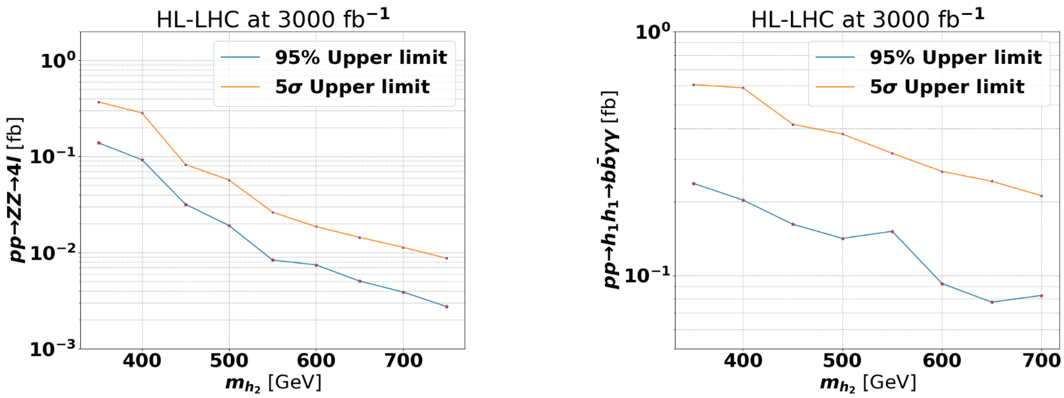

Figure 5. The HL-LHC prospective 95% CL_s upper limits and 5σ discovery limit on the production cross-sections times branching ratios for the two channels. We assume systematic uncertainty for all the backgrounds.

With these distributions and efficiencies in hand, we show in figure 5 the derived the expected 95% CL_s upper limit for the two individual channels assuming the zero background systematic uncertainties obtained with the python package `pyhf` [70, 71]. For the discovery limits, we demand that the Gaussian significance converted by the p_0 value for the background-only test to be larger than 5 given an observation of the signal plus background predicted in the model in future experiments. In the right plot in figure 5, we also plot the discovery limit contours for a combined search for different masses of h_2 on the $\sigma_{h_2 \to VV \to 4\ell}$ vs. $\sigma_{h_2 \to h_1 h_1 \to bb\gamma\gamma}$ plane. These contours are obtained `pyhf` assuming an uncorrelated signal and background for the two channels.

6 Sensitivity and exclusion limits analysis

As has been well-studied in earlier work and confirmed in the present analysis, there exists a wide range of xSM parameters compatible with a SFOEWPT. As shown in figure 2, the

JHEP12(2023)018

SFOEWPT-compatible choices can lead to non-trivial correlations between $\sigma_{h_2 \to VV \to 4\ell}$ and $\sigma_{h_2 \to h_1 h_1 \to bb\gamma\gamma}$, particularly for the region for smaller cross sections. On the other hand, for the larger values of $\sigma_{h_2 \to VV \to 4\ell}$ this correlation evaporates. Generally, for a fixed resonance mass, the 4ℓ and $bb\gamma\gamma$ cross sections are determined by $\sin\theta$ and g_{211} respectively. Therefore, for a fixed resonance mass, $\sigma_{4\ell}$ will vary over a range due to the allowed range for $\sin\theta$. The cross sections would distribute from a minimum and a maximum that are labeled by $\sigma_{4\ell}^{\min}$ and $\sigma_{4\ell}^{\max}$. Similarly, for a fixed resonance mass and a fixed 4ℓ cross section, the $bb\gamma\gamma$ cross section is not determined and locates between the maximam $\sigma_{4\ell;bb\gamma\gamma}^{\max}$ and the minimum $\sigma_{4\ell;bb\gamma\gamma}^{\min}$.

In order to carry out a systematic analysis of the LHC reach in this parameter space, we adopt the following procedure. For each resonance mass point, a set of $\sigma_{h_2 \to VV \to 4\ell}$ points are selected, which cover the full range between $\sigma_{4\ell}^{\min}$ to $\sigma_{4\ell}^{\max}$ and distribute uniformly. Then for each fixed $\sigma_{h_2 \to VV \to 4\ell}$ point, we choose two parameter sets, corresponding to the maximum value, $\sigma_{4\ell;bb\gamma\gamma}^{\max}$, and minimum value, $\sigma_{4\ell;bb\gamma\gamma}^{\min}$, respectively. In total, for each mass point, overall 30∼40 $\sigma_{h_2 \to VV \to 4\ell}$ points are selected, which results from 60∼80 number of points on the $\sigma_{h_2 \to VV \to 4\ell}$ and $\sigma_{h_2 \to h_1 h_1 \to bb\gamma\gamma}$ plane.

Figure 6 shows the prospective discovery significance for HL-LHC with 3 ab^{-1} integrated luminosity, from the $VV \to 4\ell$ channel, and from the $h_1 h_1 \to bb\gamma\gamma$ channel with maximum and minimum cross-section, respectively. The $h_1 h_1 \to bb\gamma\gamma$ channel with a maximum cross-section (red region in the left plot) has, on average larger sensitivity than the minimum cross-section (red region in the right plot). Compared to the $h_1 h_1 \to bb\gamma\gamma$, the $VV \to 4\ell$ channel (blue region) has better sensitivity, particularly for higher mass resonance signals. The $VV \to 4\ell$ channel can reach to 5-sigma discovery significance over a wide mass range from 300 GeV to 750 GeV.

It is worth emphasizing that the $VV \to 4\ell$ sensitivity is generic for any heavy Higgs that has a VV decay mode and is not specific to the xSM model. Thus, the observation of this mode at a given mass with the significance indicated would be compatible with the SFOEWPT in the xSM but not conclusive. Conversely, the non-observation of this mode would preclude the SFOEWPT-viable xSM with a heavy resonance in a significant portion of parameter space.

On the other hand, the $h_1 h_1 \to bb\gamma\gamma$ channel would provide a diagnostic probe with some sensitivity up to around 500 GeV. In terms of exclusions corresponding to the 2-sigma line on the plots, both $h_1 h_1 \to bb\gamma\gamma$ and $VV \to 4\ell$ channels have some sensitivity. In order to enhance the analysis sensitivity, results from the two channels are therefore combined. The combined discovery significance is shown in figure 7. More than half of the considered phase space points can be excluded at HL-LHC with 3 ab^{-1} integrated luminosity. On the other hand, there are also points below the 1σ line on the plots, which can be further investigated at future colliders.

One may also interpret the results discovery or exclusion regions in the plane of g_{211} and $\sin\theta$, as shown in figure 8. From left to right, these plots illustrate the HL-LHC discovery/exclusion potential for — 400±10 GeV, 550±10 GeV, 700±10 GeV respectively. All points generate SFOEWPT and satisfy requirements discussed in section 4. Constraints from Higgs measurement at LHC Run II are labeled by grey shadow. Upper limits with 95%

JHEP12(2023)018

C.L. and 5σ significance for the 4ℓ channel are given in all panels. Only the 95% C.L. upper limit for the $bb\gamma\gamma$ channel is presented in the first two panels due to its relatively weaker probing ability. Points located on the right side of each line would be observed/excluded. The plots manifest that the 4ℓ channel shows a much stronger observation/exclusion reach than the $bb\gamma\gamma$ channel, especially for heavy resonance masses.

In more detail: the blue curves and black curves represent the 5σ discovery bound and 95% CL_s exclusion bound for the $ZZ \to 4\ell$ channel. The parameter space at the right-hand side of the blue curves with bigger $|\sin\theta|$ and $|g_{211}|$ can be discovered with 5σ significance at HL-LHC if the nature is realized by the real singlet model, and the parameter spaces at the right-hand side of the black curves can be excluded with non-observation of the signal. The green and red curves are for 5σ discovery bound and 95% CL_s exclusion bound for the $h_1h_1 \to bb\gamma\gamma$ channel. All these bounds assume an integrated luminosity of $3000\,\mathrm{fb}^{-1}$. In the plot for $m_{h_2} = 700\,\mathrm{GeV}$, only the blue, black and red curves exist in the parameter space of interest because the $bb\gamma\gamma$ has no detection capability for this mass region. The shaded regions in each plot are excluded by current LHC Run-II results.

With these results in mind, one can anticipate several possible experimental outcomes:

(i) Both modes are observed: if both modes with a resonance mass $\lesssim 500\,\mathrm{GeV}$ (figure 6) are observed by 2σ, or the 4ℓ channel reaches 5σ with the $bb\gamma\gamma$ reaching 2σ, it is expected by, and shows strong evidence for, the SFOEWPT-viable xSM. However, observation of both channels by 5σ would be inconsistent with the SFOEWPT-viable xSM except for $m_{h_2} \sim 350\,\mathrm{GeV}$.

(ii) Neither channel is observed at the HL-LHC: the non-observation of both the 4ℓ and di-Higgs channels does not rule out the SFOEWPT-viable xSM. However, it implies an intriguing pattern regarding the sign correlation between $\sin\theta$ and g_{211}. Notably, for parameter points remaining unexcluded by the future HL-LHC experiment, a negative $\sin\theta$ is only consistent with a relatively light h_2 mass. Additionally, in cases of negative $\sin\theta$, there is a strong correlation between g_{211} and $\sin\theta$, as indicated by the narrow strip in the left plot of figure 9. We discuss this correlation and figure 9 in more detail below.

(iii) The $VV \to 4\ell$ is observed but the $h_1h_1 \to bb\gamma\gamma$ is not: if the observed resonance satisfies $\gtrsim 350\,\mathrm{GeV}$, the existence of a heavy resonance compatible with the SFOEWPT-xSM would be established but a future more sensitive search for the $h_1h_1 \to bb\gamma\gamma$ would be needed. On the other hand, if the resonance is $\lesssim 350\,\mathrm{GeV}$, the observation would be in consistent with xSM prediction and is hence ruled out.

(iv) The $h_1h_1 \to bb\gamma\gamma$ is observed but the $VV \to 4\ell$ is not: if one observes the di-Higgs channel with $bb\gamma\gamma$ final states in the small resonance mass region ($\lesssim 350\,\mathrm{GeV}$) and no significant observations for the 4ℓ channel, the result would be consistent with the SFOEWPT in the xSM. On the contrary, if the observation occurs with heavier-mass resonance ($\gtrsim 500\,\mathrm{GeV}$), the SFOEWPT-viable xSM prediction would be inconsistent with the observation and, therefore, the xSM FOEWPT would be ruled out.

JHEP12(2023)018

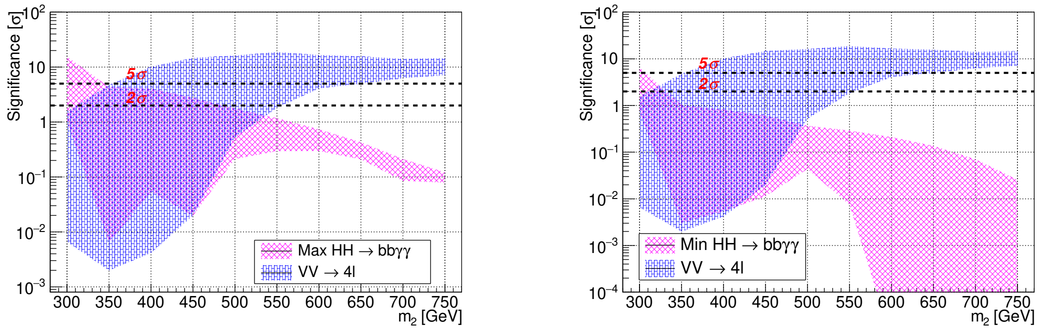

Figure 6. Prospective discovery/exclusion reach for HL-LHC with 3 ab^{-1}. Horizontal and vertical axes give heavy scalar mass and significance, respectively. Red points in the left (right) panels indicate range of maximum (minimum) $\sigma_{h_1 h_1 \to bb\gamma\gamma}$ as one varies over the range of $\sigma_{VV\to 4l}$. The significance for the latter is indicated by the blue points. For a fixed M_S, $\sigma_{VV\to 4l}$ depends mainly on $\sin\theta$ mainly. All points satisfy the requirement of SFOEWPT.

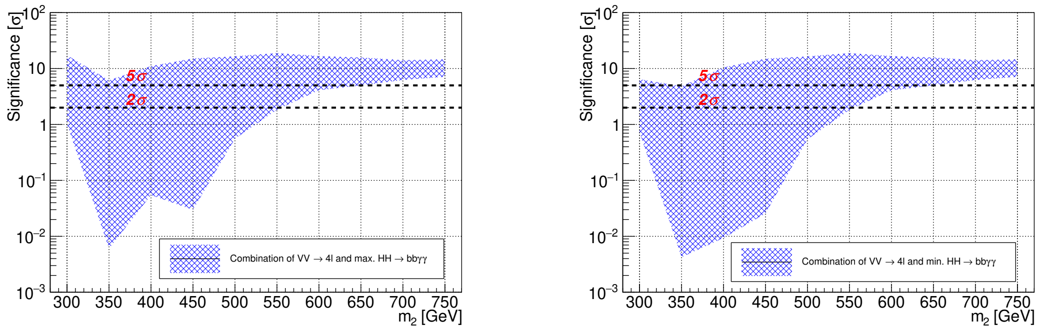

Figure 7. Prospective discovery/exclusion reach for HL-LHC with 3 ab^{-1} from the combination of two channels: (1) the $VV \to 4\ell$ channel, and (2) $h_1 h_1 \to bb\gamma\gamma$ channel with maximum cross section (left panel) and with minimum cross section (right panel).

Note that for each possible outcome, one would need to perform an updated xSM parameter scan that takes into account the various experimental results.

We now comment further on the question of the sign of $\sin\theta$ and the correlation with other xSM tri-scalar couplings. First, we observe that the independent measurement of the sign of $\sin\theta$ is not an easy task, and one cannot determine the sign of $\sin\theta$ with solely the couplings between h_2 and SM fermions or vector bosons, because in this case each propagator of h_2 present in a diagram must contribute to 2 powers of $\sin\theta$ erasing the sign information. In this case, the sign of the $\sin\theta$ must be resolved by a global fit that includes physical processes that are sensitive to all the scalar couplings, such as g_{221}. As an illustration, in figure 9, we show the scatter plot in the g_{211} vs g_{221} plane for all the points that can give SFOEWPT and simultaneously satisfy all the theoretical and current experimental bounds, including the one from LHC run-II. The color of the points indicates the sign of the mixing angle $\sin\theta$, red for positive and blue for negative. One can find that for m_{h_2} around 400 GeV, the points with the different sign of $\sin\theta$ tend to populate different parameter space in this 2-D plane, which indicates that the measurement of the two tri-linear couplings could help to disentangle the sign of $\sin\theta$ in xSM.

JHEP12(2023)018

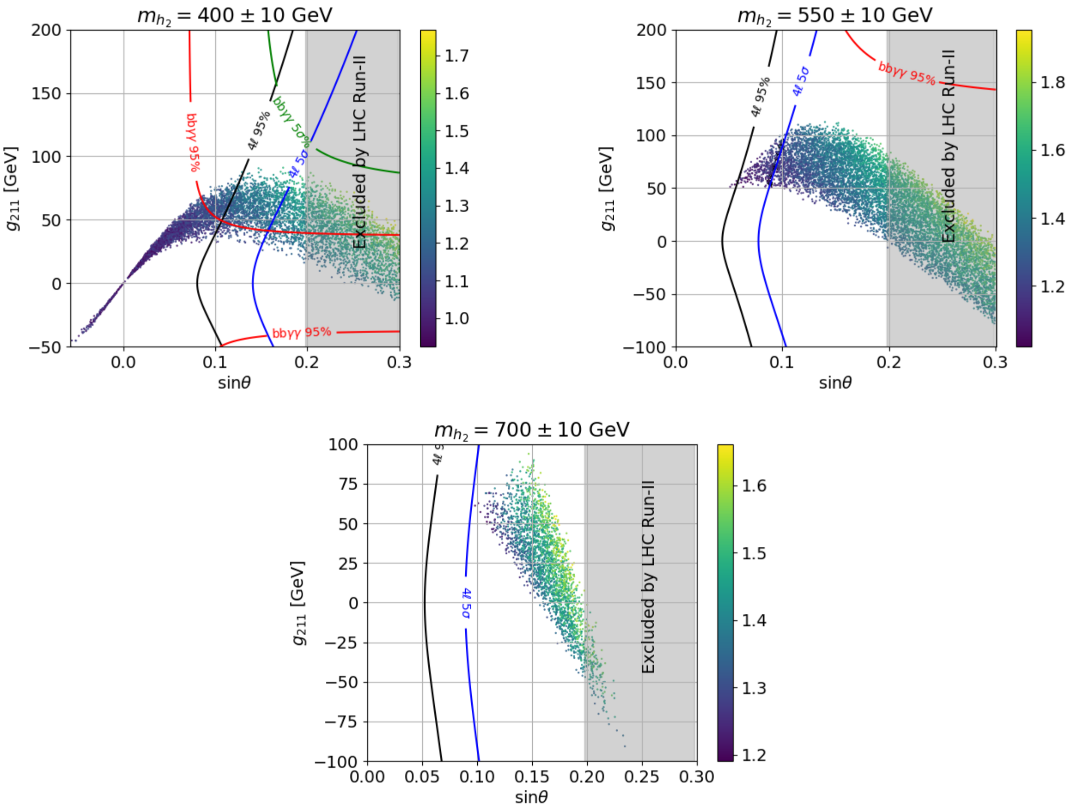

Figure 8. Prospective HL-LHC (3 ab^{-1}) discovery and exclusion reaches for the coupling g_{211}/GeV as a function of $\sin\theta$ allowed by the SFOEWPT for 400 GeV (the first panel), 550 GeV (the second panel) and 700 GeV (the third panel) resonance masses. Color bars in the panels correspond to the ratio of $g_{111}/g_{111}^{\rm SM}$. The area to the right of each line corresponds to the discovery/exclusion reach for a given channel. The solid lines represent HL-LHC exclusion bound as labeled above The grey region is excluded by LHC Run-II. All the points in the plot satisfy theoretical bounds and survive from the EWPT discussed in section 4.

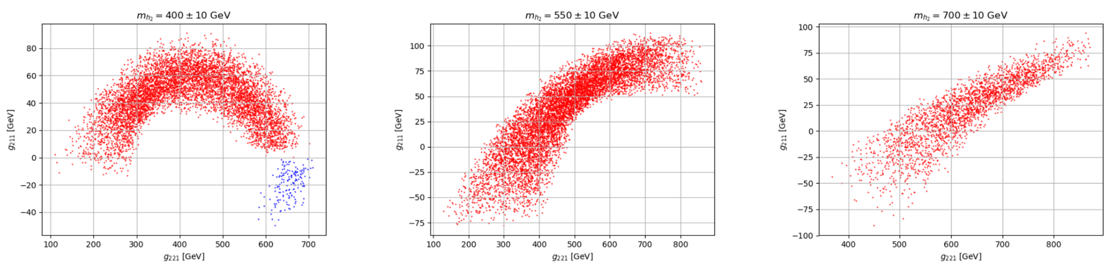

Figure 9. Points in the g_{211} vs g_{221} plane, where we have removed the points that are excluded by current LHC measurements. The red (blue) color indicates that the sign of $\sin\theta$ for the corresponding point is positive (negative).

7 Conclusion

Exploring the thermal history of electroweak symmetry breaking is an important effort in its own right and may yield clues to solving the baryogenesis problem through EWBG. This scenario requires a SFOEWPT as a pre-condition for generation of the CPV asymmetries that ultimately yield the baryon asymmetry. In the SM, EWSB occurs though a cross-over transition. However, the Higgs portal interactions in the xSM can generate a SFOEWPT for suitable choices of model parameters. The portal interactions are strongly correlated with the strength of the EWPT. Generally, a successful SFOEWPT requires relatively large portal interactions. However, constraints from Higgs measurement, EWPO and perturbativity indicate that the magnitudes of the mixing angle and the portal couplings cannot be arbitrarily large. Therefore, the parameter space is highly constrained. Through our analysis, we find that the remained parameter space has different sensitivies for different detection channels. As is well-known, one of the effective ways to detect the Higgs portal interactions is the heavy scalar resonance search via di-Higgs channel. For the di-Higgs channel, we have considered in particular the $bb\gamma\gamma$ final state. Another way to probe the Higgs portal interactions is through the di-boson channel. For the di-boson channel, we have considered in particular the 4ℓ final state. A novel aspect of this study is the analysis of the complementarity between these two channels and the discovery/exclusion reach that results from their combination.

Through our analysis We find that the $b\bar{b}\gamma\gamma$ channel is able to explore the low mass region with $m_2 \lesssim 320\,\text{GeV}$ effectively and the 4ℓ channel is more suitable for the high mass region with $m_2 \gtrsim 500\,\text{GeV}$. It is also possible that a combination of the two search channels can push the significance above 5σ even though the significance for each individual channel is less than 5σ. In terms of exclusion, one is able to exclude the portion of SFOEWPT parameter space by taking advantage of the combination of $b\bar{b}\gamma\gamma$ and 4ℓ channels over roughly $m_2 \lesssim 750\,\text{GeV}$ at the $14\,\text{TeV}$ HL-LHC with luminosity $3ab^{-1}$. Moreover, the combination of both channels provides an important diagnostic probe of the SFOEWPT-viable xSM. However, signal events associated with minimal $b\bar{b}\gamma\gamma$ cross section are difficult to exclude at the HL-LHC, pointing to the need for a future collider with higher energy to obtain a comprehensive probe (see, e.g., refs. [13, 16]). Finally, in the case of combined discovery, there is a strong correlation between g_{211} and $\sin\theta$. On the other hand, even though a non-observation of both channels would not rule out SFOEWPT-viable xSM, it would put constraints on the sign of the mixing angle and the tri-linear scalar coupling g_{211}. In this case, future high-energy collider experiments may needed to further diagnose and probe the different scalar couplings in the model (see, e.g., refs. [13, 16]). We show as an example how the simultaneous measurement of g_{211} and g_{221} could allow one to disentangle the sign of $\sin\theta$ in the SFOEWPT-viable xSM.

Acknowledgments

SA, MJRM and WZ are supported in part under National Natural Science Foundation of China grant No. 11975150. H.-L.L. is supported by F.R.S.-FNRS through the IISN convention “Theory of Fundamental Interactions” (N: 4.4517.08). KL is supported by the Major International (Regional) Joint Research Program of NSFC-CERN (Grant No.12061141004).

A Supplementary materials

A.1 Two-loop β-functions for the dimensionless parameters

We use the python package `PyR@TE 3` [72] to derive the renormalization group equations (RGEs) in the $\overline{\text{MS}}$ scheme at one-loop level and checked that the results in the limiting cases are in agreement with those in literatures [73–76]. The full one-loop RGEs in the form of $\mathrm{d}X/\mathrm{d}\log\mu = \beta^{(1)}(X)/(4\pi)^2$ are given as follows:

$$\beta^{(1)}(g_1) = \frac{41}{6} g_1^3 \tag{A.1}$$

$$\beta^{(1)}(g_2) = -\frac{19}{6} g_2^3 \tag{A.2}$$

$$\beta^{(1)}(g_3) = -7 g_3^3 \tag{A.3}$$

$$\beta^{(1)}(y_t) = +\frac{9}{2} y_t |y_t|^2 + \frac{3}{2} y_t |y_b|^2 - \frac{17}{12} g_1^2 y_t - \frac{9}{4} g_2^2 y_t - 8 g_3^2 y_t \tag{A.4}$$

$$\beta^{(1)}(y_b) = +\frac{9}{2} y_b |y_b|^2 + \frac{3}{2} y_b |y_t|^2 - \frac{5}{12} g_1^2 y_b - \frac{9}{4} g_2^2 y_b - 8 g_3^2 y_b \tag{A.5}$$

$$\begin{aligned}\beta^{(1)}(\lambda) = &+ 24\lambda^2 + \frac{1}{2} a_2^2 - 3 g_1^2 \lambda - 9 g_2^2 \lambda + \frac{3}{8} g_1^4 + \frac{3}{4} g_1^2 g_2^2 + \frac{9}{8} g_2^4 \\ &+ 12\lambda |y_t|^2 + 12\lambda |y_b|^2 - 6 |y_t|^4 - 6 |y_b|^4\end{aligned} \tag{A.6}$$

$$\beta^{(1)}(a_2) = + 12 a_2 \lambda + 4 a_2^2 + 6 a_2 b_4 - \frac{3}{2} a_2 g_1^2 - \frac{9}{2} a_2 g_2^2 + 6 a_2 |y_t|^2 + 6 a_2 |y_b|^2 \tag{A.7}$$

$$\beta^{(1)}(b_4) = + 2 a_2^2 + 18 b_4^2 \tag{A.8}$$

$$\begin{aligned}\beta^{(1)}(a_1) = &- \frac{3}{2} a_1 g_1^2 - \frac{9}{2} a_1 g_2^2 + 12 a_1 \lambda + 4 a_1 a_2 + 4 a_2 b_3 \\ &+ 6 a_1 |y_t|^2 + 6 a_1 |y_b|^2 + 2 a_1 |y_\tau|^2\end{aligned} \tag{A.9}$$

$$\beta^{(1)}(b_3) = + 3 a_1 a_2 + 18 b_3 b_4 \tag{A.10}$$

$$\begin{aligned}\beta^{(1)}(\mu^2) = &- \frac{3}{2} g_1^2 \mu^2 - \frac{9}{2} g_2^2 \mu^2 - \frac{1}{2} a_1^2 + 12\lambda\mu^2 - a_2 b_2 \\ &+ 6\mu^2 |y_t|^2 + 6\mu^2 |y_b|^2 + 2\mu^2 |y_\tau|^2\end{aligned} \tag{A.11}$$

$$\beta^{(1)}(b_2) = + a_1^2 + 4 b_3^2 - 4 a_2 \mu + 6 b_2 b_4, \tag{A.12}$$

where g_1, g_2, g_3 are $\mathrm{U}(1)_y$, $\mathrm{SU}(2)_L$ and $\mathrm{SU}(3)_c$ gauge couplings respectively and y_t and y_b are Yukawa couplings for top and bottom quarks. Their definitions are summarized in the following equations:

$$D_\mu \Psi = (\partial_\mu - i g_1 q B_\mu - i g_2 T_2^i W_\mu^i - i g_3 T_3^a G^a)\Psi, \tag{A.13}$$

$$\mathcal{L}_{\text{Yukawa}} = y_t \bar{Q}_L \tilde{H} u_R + y_b \bar{Q}_L H d_R + h.c., \tag{A.14}$$

where q is the $\mathrm{U}(1)_y$ charge of the field Ψ, T_2 and T_3 are the corresponding generators of the SU(2) and SU(3) groups depending on the representations of the field Ψ. For example, for the quark left-handed doublet Q_L, it has $q = 1/6$, $T_2^2 = \sigma^i/2$ and $T_3^a = \lambda^a/2$ with σ^i and λ^a

JHEP12(2023)018

the Pauli and Gell-Mann matrices respectively. $\tilde{H}_i \equiv i\sigma^2_{ij} H_j$, u_R and b_R are right-handed up-type and down-type quark singlets respectively.

For the initial inputs of SM Yukawa and gauge couplings g_1, g_2, g_3, y_t, y_b, we use the package `mr` [77] to convert the input parameters from the On-Shell scheme to the $\overline{\text{MS}}$ scheme and run to the scale $\mu = 246\,\text{GeV}$. When converting between the On-shell and $\overline{\text{MS}}$ scheme, we use the relations in the order of one-loop QCD and EW in the Standard model and assume that the correction from the heavy Higgs is small provided that the $\sin\theta$ is within the constraint of EWPO. For the running couplings g_1, g_2, g_3, y_t, y_b, we implement the one-loop RGEs for consistency, which is not affected by the heavy singlet in xSM. The On-Shell input parameters are obtained from the Particle Data Group [62]:

$$M_b = 4.78\,\text{GeV}, \quad M_t = 172.69\,\text{GeV}, \quad M_W = 80.377\,\text{GeV}, \quad M_Z = 91.1876\,\text{GeV}, \tag{A.15}$$

$$M_h = 125.25\,\text{GeV}, \quad G_F = 1.16638\,\text{GeV}^{-2}, \quad \alpha_s(M_t) = 0.108102, \tag{A.16}$$

from which we obtain the $\overline{\text{MS}}$ couplings at the scale $\mu = 246\,\text{GeV}$ as follows:

$$g_1 = 0.36001, \qquad g_2 = 0.64632, \qquad g_3 = 1.15330, \tag{A.17}$$

$$y_t = 0.93930, \qquad y_b = 0.01897. \tag{A.18}$$

A.2 bb$\gamma\gamma$ channel simulation

We perform a generation of a signal process $pp \to h_2 \to h_1 h_1 \to b\bar{b}\gamma\gamma$ by utilizing MadGraph5 [78] in parton level and use Pythia8 [79] to simulate the parton shower process followed by a detector simulating software Delphes3 [80] to simulate the detector response of this process at LHC. In this section, we will follow the ATLAS analysis in ref. [26] and reproduce the cutflow efficiency compared with the experimental data.

In the detector simulation, photon candidates must satisfy isolation criteria of $\Delta R \leq 0.2$ for both calorimeter- and track-based isolation. In track-based isolation, the transverse momentum within the cone (p_T^{iso}) counts only the tracks with $p_T > 1\,\text{GeV}$. Jets are reconstructed using anti-k_t clustering algorithm [81] with a radius parameter set to be $R = 0.4$ and are required to satisfy $|\eta| < 2.5$ and $p_T > 25\,\text{GeV}$. In addition, the efficiency for a b-quark jet to pass the b-tagging requirement is set to be a constant equal to 70% [82] approximately.

The selection is simplified according to ref. [26]:

- Events are required to have at least two photons and two jets with one or two jets recognized as b-jet(s). Any event containing more than two b-jets is rejected.
- The invariant mass of two photon with the highest p_T should satisfy $105\,\text{GeV} < m_{\gamma\gamma} < 160\,\text{GeV}$.
- For each photon, it is required to have $E_T/m_{\gamma\gamma} > 0.35$ and 0.25 respectively.
- Four signal regions are defined based on the highest-p_T and next-highest p_T(They are called "Cen Jets" in table 3). If $p_T^1 > 40$GeV and $p_T^2 > 25$GeV, the signal is labeled with "loose". If $p_T^1 > 100$GeV and $p_T^2 > 30$GeV, the signal is labeled "tight".

	$m_{\gamma\gamma}$	2 Cen Jets	b-tagging	bjet pT	m_{bb}	$E_T/m_{\gamma\gamma}$
Exp(300GeV 1-btag)	37.6%	27.80%	11.8%	10.8%	5.9%	5.6%
Sim(300GeV 1-btag)	37.6%	27.9%	12.65%	9.56%	5.52%	5.39%
Exp(300GeV 2-btag)	37.6%	27.8%	8.1%	7.9%	6.8%	6.4%
Sim(300GeV 2-btag)	37.6%	27.9%	7.63%	7.09%	5.84%	5.82%
Exp(400GeV 1-btag)	40.2%	32.8%	14.3%	5.5%	2.5%	2.4%
Sim(400GeV 1-btag)	40.2%	32.7%	13.44%	5.42%	1.98%	1.98%
Exp(400GeV 2-btag)	40.2%	32.8%	10.3%	4.3%	3.6%	3.4%
Sim(400GeV 2-btag)	40.2%	32.7%	12.05%	4.85%	3.70%	3.70%

Table 3. Cutflows for higgs production at LHC with $\sqrt{s} = 1.3\,\text{TeV}$, $m_{h_2} = 300/400\,\text{GeV}$, $\mathcal{L} = 250 fb^{-1}$. The Exp-line shows the experimental result in ref. [26]. The Sim-line shows the simulation result.

Combining with the b-jet number, signal events are classified to four regions, which are "1-btag loose", "1-btag tight", "2-btag loose" and "2-btag tight".

- For tight (loose) signal regions, the diphoton invariant mass is required to be $125\,\text{GeV} \pm 4.3(4.7)$ GeV.
- The dijet system is rescaled by a factor of m_H/m_{jj}.
- Loose selection is used for resonances with $m_X \leq 400\,\text{GeV}$ and the tight selection for resonances with $m_X \geq 400\,\text{GeV}$. For tight (loose) selection, we require 335 GeV $< m_{\gamma\gamma jj} < 1140\,\text{GeV}$($245\,\text{GeV} < m_{\gamma\gamma jj} < 610\,\text{GeV}$).
- For events that pass the selection above, we obtain their $m_{bb\gamma\gamma}$ distribution.

A.3 $ZZ \to 4\ell$ channel simulation and selection

We generate the parton level signal events $pp \to h_2 \to ZZ \to \ell^+\ell^-\ell^+\ell^-$ with MadGraph5 [78], then showering with Pythia8 [79] and simulate the detector effect with Delphes3 [80]. We follow the ATLAS analysis in ref. [22], and reproduce similar signal and background efficiencies in that paper. The analysis cut flow is described as followings:

- Select the events with two same-flavor opposite-sign lepton pairs. The reconstructed electron (muon) must have $p_T > 7(5)$ GeV and $|\eta| < 2.47(2.7)$.
- For lepton pairs, we denote the invariant mass of the pair closer to Z mass as m_{12} and that of the other pair as m_{34}. We demand that m_{12} and m_{34} satisfying the following cuts:

$$\begin{aligned} 50\,\text{GeV} < m_{12} < 106\,\text{GeV} \\ m_{34} < 116\,\text{GeV} \\ m_{34} > \begin{cases} 12\,\text{GeV} & m_{4\ell} \leq 140\ \text{GeV} \\ 12 + 50\frac{m_{4\ell}-140}{190-140} & 140\ \text{GeV} < m_{4\ell} < 190\,\text{GeV} \\ 50\,\text{GeV} & m_{4\ell} \geq 190\,\text{GeV} \end{cases} \end{aligned} \tag{A.19}$$

	Sim (600 GeV)	Exp (600 GeV)
4μ	42.2%	48%
$4e$	63.4%	64%
$2\mu 2e$	51.7%	57%

Table 4. Signal efficiencies for different lepton channels of the process the $h_2 \to ZZ \to 4\ell$, the Exp numbers are obtained from ref. [22].

- We also require that leptons are separated with each other by $\Delta R > 0.1$ if they are the same flavor, and $\Delta R > 0.2$ otherwise.
- For 4μ and $4e$ events, we veto the events containing opposite-sign lepton pairs with $m_{\ell\ell} < 5$ GeV.
- We implement the cut on the track-isolation discriminant as the sum of the transverse momenta of tracks within $\Delta R = 0.3$ (0.2) of the muon (electron) candidate excluding the lepton track, divided by the p_T of the lepton. Such discriminants are required to be smaller than 0.15.

Compared to ref. [22], we did not impose the calorimeter-based isolation requirement because they are technically difficult to implement in the Delphes. In practice„ we find that the major effect on the signal efficiencies is from the detector efficiencies for leptons, and with the above cuts we are already able to obtain signal efficiencies reasonably close to those in the ATLAS paper [22]. In table 4, we illustrate the effectiveness of our simulation by showing the comparison of signal efficiencies for different lepton channels for a fixed benchmark point $m_{h_2} = 600$ GeV, we only compare the final efficiencies because the efficiencies for the intermediate cuts are inaccessible in the experimental paper.

A.4 Comments on the constraint from electroweak precision observables (EWPO)

xSM can influence EWPO in two ways: rescaling couplings between the SM-like Higgs to SM particles and generating new diagrams involving the single-like Higgs. When parameterizing theoretical predictions of EWPO in the framework of the oblique parameters S, T and U [83, 84], the shifted oblique parameters in the xSM can be uniquely determined by the two physical parameters: the mixing angle θ and the mass of the singlet-like Higgs m_2, which can be expressed in the following formula,

$$\Delta\mathcal{O} = (\cos^2\theta - 1)\mathcal{O}^{\rm SM}(m_{h_1}) + \sin^2\theta\mathcal{O}^{\rm SM}(m_{h_2}) = \sin^2\theta\left[\mathcal{O}^{\rm SM}(m_{h_2}) - \mathcal{O}^{\rm SM}(m_{h_1})\right], \tag{A.20}$$

where $\mathcal{O}$ can be either S, T or U, and $\mathcal{O}^{\rm SM}(m_{h_2})$ are the SM expression for $\mathcal{O}$ if the Higgs mass were to be m_{h_2}. Therefore a constraint on the $\cos\theta - m_{h_2}$ plane can be derived by constructing the χ^2 with the predicted oblique observables and the experimental data. In our previous work [35], we used the global fitted center values, uncertainties, and correlations for these oblique parameters from the Gfitter group [85] and obtained a lower bound on $\cos\theta$ as a function of m_{h_2}. However, the recently updated measurement of m_W from the CDF collaboration [86] exhibits a significant deviation from the SM prediction, which indicates a qualitative change in the EWPO constraint for xSM.

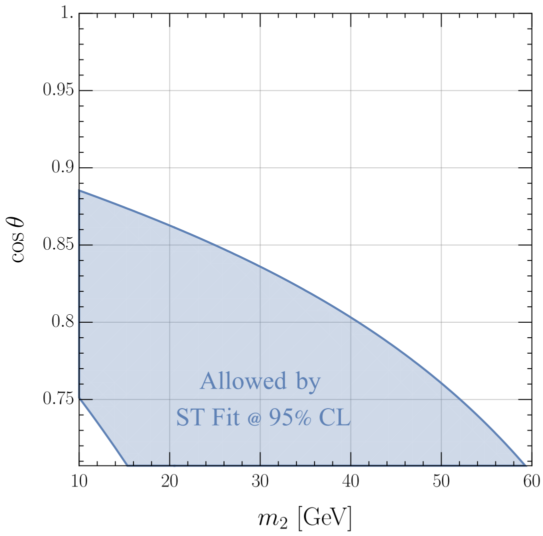

Figure 10. The allowed parameter space at 95% CL for xSM using the global fit from ref. [87] assuming $U = 0$ and M_W with conservative average. The vertical axis start from $\theta = \pi/4$, above which the mass eigenstate h_1 gets more contribution from the neutral part in the Higgs doublet thus corresponding to the SM-like Higgs.

To illustrate the potential influence of such a new m_W measurement on the EWPO constraint for xSM, we follow the recent global fit result by the `HEPfit` group [87], where they combine the measurements from LEP2, LHC and Tevatron including the most recent CDFII results to give a new "world average" of W mass as:

$$m_W = 80.4133 \pm 0.0080 \; (0.015) \, \text{GeV}, \tag{A.21}$$

where the number in the parenthesis represents an inflated error for a conservative average. From this updated value of m_W, authors in ref. [87] derive four sets of constraints on the S, T, and U parameters assuming whether one uses the conservative average or not and whether one sets $U = 0$ or not. As an example, we plot the allowed parameter space at 95% confidence level (CL) in the $\cos\theta - m_{h_2}$ plane in the blue region in figure 10 assuming $U = 0$ and m_W taking the conservative average, which corresponds to the following bounds and correlations matrix on the S and T parameters:

$$\Delta S = 0.086 \pm 0.077, \qquad \Delta T = 0.177 \pm 0.070, \tag{A.22}$$

$$\rho = \begin{pmatrix} 1 & 0.89 \\ 0.89 & 1 \end{pmatrix}. \tag{A.23}$$

One can find that the allowed parameter space tends to have a very small m_{h_2} such that the diHiggs decay channel is not available. This is expected, since the updated W boson mass from CDFII indicates a relatively large violation of custodial symmetry, while xSM scalar potential does not explicitly break the custodial symmetry, as a consequence, the new physics contribution to the custodial symmetry breaking starts at one-loop receiving a loop factor suppression, to compensate such a suppression one needs a relatively small singlet-like Higgs mass. However, we need to emphasize here that the above global analysis

JHEP12(2023)018

heavily depends on the method used for combining the W mass measurements from different experiments, given that the newly measured m_W has a significant discrepancy compared with all the previous measurements, the ordinary averaging method assuming correlated Gaussian uncertainties may not be appropriate anymore, and the community has not reached a common agreement on the interpretation of the experimental results yet.

References

[1] ATLAS collaboration, *Observation of a new particle in the search for the Standard Model Higgs boson with the ATLAS detector at the LHC*, Phys. Lett. B **716** (2012) 1 [arXiv:1207.7214] [INSPIRE].

[2] CMS collaboration, *Observation of a New Boson at a Mass of 125 GeV with the CMS Experiment at the LHC*, Phys. Lett. B **752** (2012) 30 [arXiv:1207.7235] [INSPIRE].

[3] Planck collaboration, *Planck 2013 results. XVI. Cosmological parameters*, Astron. Astrophys. **571** (2014) A16 [arXiv:1303.5076] [INSPIRE].

[4] V.A. Kuzmin, V.A. Rubakov and M.E. Shaposhnikov, *On the Anomalous Electroweak Baryon Number Nonconservation in the Early Universe*, Phys. Lett. B **155** (1985) 36 [INSPIRE].

[5] M.E. Shaposhnikov, *Possible Appearance of the Baryon Asymmetry of the Universe in an Electroweak Theory*, JETP Lett. **44** (1986) 465 [INSPIRE].

[6] M.E. Shaposhnikov, *Baryon Asymmetry of the Universe in Standard Electroweak Theory*, Nucl. Phys. B **287** (1987) 757 [INSPIRE].

[7] A.G. Cohen, D.B. Kaplan and A.E. Nelson, *Progress in electroweak baryogenesis*, Ann. Rev. Nucl. Part. Sci. **43** (1993) 27 [hep-ph/9302210] [INSPIRE].

[8] D.E. Morrissey and M.J. Ramsey-Musolf, *Electroweak baryogenesis*, New J. Phys. **14** (2012) 125003 [arXiv:1206.2942] [INSPIRE].

[9] A.D. Sakharov, *Violation of CP Invariance, C asymmetry, and baryon asymmetry of the universe*, Pisma Zh. Eksp. Teor. Fiz. **5** (1967) 32 [INSPIRE].

[10] K. Kajantie, M. Laine, K. Rummukainen and M.E. Shaposhnikov, *A Nonperturbative analysis of the finite T phase transition in* SU(2) × U(1) *electroweak theory*, Nucl. Phys. B **493** (1997) 413 [hep-lat/9612006] [INSPIRE].

[11] F.R. Klinkhamer and N.S. Manton, *A Saddle Point Solution in the Weinberg-Salam Theory*, Phys. Rev. D **30** (1984) 2212 [INSPIRE].

[12] K. Kajantie, M. Laine, K. Rummukainen and M.E. Shaposhnikov, *Is there a hot electroweak phase transition at $m_H \gtrsim m_W$?*, Phys. Rev. Lett. **77** (1996) 2887 [hep-ph/9605288] [INSPIRE].

[13] M.J. Ramsey-Musolf, *The electroweak phase transition: a collider target*, JHEP **09** (2020) 179 [arXiv:1912.07189] [INSPIRE].

[14] D. O'Connell, M.J. Ramsey-Musolf and M.B. Wise, *Minimal Extension of the Standard Model Scalar Sector*, Phys. Rev. D **75** (2007) 037701 [hep-ph/0611014] [INSPIRE].

[15] S. Profumo, M.J. Ramsey-Musolf and G. Shaughnessy, *Singlet Higgs phenomenology and the electroweak phase transition*, JHEP **08** (2007) 010 [arXiv:0705.2425] [INSPIRE].

[16] A.V. Kotwal, M.J. Ramsey-Musolf, J.M. No and P. Winslow, *Singlet-catalyzed electroweak phase transitions in the* 100 *TeV frontier*, Phys. Rev. D **94** (2016) 035022 [arXiv:1605.06123] [INSPIRE].

[17] K. Hashino et al., *Gravitational waves and Higgs boson couplings for exploring first order phase transition in the model with a singlet scalar field*, Phys. Lett. B **766** (2017) 49 [arXiv:1609.00297] [INSPIRE].

[18] ATLAS collaboration, *Search for pair production of Higgs bosons in the $b\bar{b}b\bar{b}$ final state using proton-proton collisions at $\sqrt{s} = 13$ TeV with the ATLAS detector*, JHEP **01** (2019) 030 [arXiv:1804.06174] [INSPIRE].

[19] CMS collaboration, *Search for resonant pair production of Higgs bosons decaying to bottom quark-antiquark pairs in proton-proton collisions at* 13 *TeV*, JHEP **08** (2018) 152 [arXiv:1806.03548] [INSPIRE].

[20] ATLAS collaboration, *Search for Higgs boson pair production in the $b\bar{b}WW^*$ decay mode at $\sqrt{s} = 13$ TeV with the ATLAS detector*, JHEP **04** (2019) 092 [arXiv:1811.04671] [INSPIRE].

[21] CMS collaboration, *Search for resonant and nonresonant Higgs boson pair production in the $b\bar{b}\ell\nu\ell\nu$ final state in proton-proton collisions at $\sqrt{s} = 13$ TeV*, JHEP **01** (2018) 054 [arXiv:1708.04188] [INSPIRE].

[22] ATLAS collaboration, *Search for heavy ZZ resonances in the $\ell^+\ell^-\ell^+\ell^-$ and $\ell^+\ell^-\nu\bar{\nu}$ final states using proton-proton collisions at $\sqrt{s} = 13$ TeV with the ATLAS detector*, Eur. Phys. J. C **78** (2018) 293 [arXiv:1712.06386] [INSPIRE].

[23] ATLAS collaboration, *Search for Higgs boson pair production in the $WW^{(*)}WW^{(*)}$ decay channel using ATLAS data recorded at $\sqrt{s} = 13$ TeV*, JHEP **05** (2019) 124 [arXiv:1811.11028] [INSPIRE].

[24] ATLAS collaboration, *Search for resonant and non-resonant Higgs boson pair production in the $b\bar{b}\tau^+\tau^-$ decay channel in pp collisions at $\sqrt{s} = 13$ TeV with the ATLAS detector*, Phys. Rev. Lett. **121** (2018) 191801 [*Erratum ibid.* **122** (2019) 089901] [arXiv:1808.00336] [INSPIRE].

[25] CMS collaboration, *Search for Higgs boson pair production in events with two bottom quarks and two tau leptons in proton-proton collisions at $\sqrt{s} = 13$ TeV*, Phys. Lett. B **778** (2018) 101 [arXiv:1707.02909] [INSPIRE].

[26] ATLAS collaboration, *Search for Higgs boson pair production in the $\gamma\gamma b\bar{b}$ final state with* 13 *TeV pp collision data collected by the ATLAS experiment*, JHEP **11** (2018) 040 [arXiv:1807.04873] [INSPIRE].

[27] CMS collaboration, *Search for Higgs boson pair production in the $\gamma\gamma b\bar{b}$ final state in pp collisions at $\sqrt{s} = 13$ TeV*, Phys. Lett. B **788** (2019) 7 [arXiv:1806.00408] [INSPIRE].

[28] ATLAS collaboration, *Search for heavy diboson resonances in semileptonic final states in pp collisions at $\sqrt{s} = 13$ TeV with the ATLAS detector*, Eur. Phys. J. C **80** (2020) 1165 [arXiv:2004.14636] [INSPIRE].

[29] ATLAS collaboration, *Search for WW/WZ resonance production in $\ell\nu qq$ final states in pp collisions at $\sqrt{s} = 13$ TeV with the ATLAS detector*, JHEP **03** (2018) 042 [arXiv:1710.07235] [INSPIRE].

JHEP12(2023)018

[30] ATLAS collaboration, *Searches for heavy diboson resonances in pp collisions at $\sqrt{s} = 13$ TeV with the ATLAS detector*, JHEP **09** (2016) 173 [arXiv:1606.04833] [INSPIRE].

[31] ATLAS collaboration, *Search for diboson resonances with boson-tagged jets in pp collisions at $\sqrt{s} = 13$ TeV with the ATLAS detector*, Phys. Lett. B **777** (2018) 91 [arXiv:1708.04445] [INSPIRE].

[32] ATLAS collaboration, *Combination of searches for heavy resonances decaying into bosonic and leptonic final states using 36 fb^{-1} of proton-proton collision data at $\sqrt{s} = 13$ TeV with the ATLAS detector*, Phys. Rev. D **98** (2018) 052008 [arXiv:1808.02380] [INSPIRE].

[33] ATLAS collaboration, *Search for heavy resonances decaying into WW in the $e\nu\mu\nu$ final state in pp collisions at $\sqrt{s} = 13$ TeV with the ATLAS detector*, Eur. Phys. J. C **78** (2018) 24 [arXiv:1710.01123] [INSPIRE].

[34] ATLAS collaboration, *Search for heavy Higgs bosons decaying into two tau leptons with the ATLAS detector using pp collisions at $\sqrt{s} = 13$ TeV*, Phys. Rev. Lett. **125** (2020) 051801 [arXiv:2002.12223] [INSPIRE].

[35] T. Huang et al., *Resonant di-Higgs boson production in the $b\bar{b}WW$ channel: Probing the electroweak phase transition at the LHC*, Phys. Rev. D **96** (2017) 035007 [arXiv:1701.04442] [INSPIRE].

[36] J.R. Espinosa, T. Konstandin and F. Riva, *Strong Electroweak Phase Transitions in the Standard Model with a Singlet*, Nucl. Phys. B **854** (2012) 592 [arXiv:1107.5441] [INSPIRE].

[37] H.H. Patel and M.J. Ramsey-Musolf, *Baryon Washout, Electroweak Phase Transition, and Perturbation Theory*, JHEP **07** (2011) 029 [arXiv:1101.4665] [INSPIRE].

[38] M. Laine, *Gauge dependence of the high temperature two loop effective potential for the Higgs field*, Phys. Rev. D **51** (1995) 4525 [hep-ph/9411252] [INSPIRE].

[39] A. Ekstedt and J. Löfgren, *On the relationship between gauge dependence and IR divergences in the $\hbar$-expansion of the effective potential*, JHEP **01** (2019) 226 [arXiv:1810.01416] [INSPIRE].

[40] M. Garny and T. Konstandin, *On the gauge dependence of vacuum transitions at finite temperature*, JHEP **07** (2012) 189 [arXiv:1205.3392] [INSPIRE].

[41] M. Carena, Z. Liu and Y. Wang, *Electroweak phase transition with spontaneous Z_2-breaking*, JHEP **08** (2020) 107 [arXiv:1911.10206] [INSPIRE].

[42] J. Kozaczuk, M.J. Ramsey-Musolf and J. Shelton, *Exotic Higgs boson decays and the electroweak phase transition*, Phys. Rev. D **101** (2020) 115035 [arXiv:1911.10210] [INSPIRE].

[43] A. Alves et al., *Collider and Gravitational Wave Complementarity in Exploring the Singlet Extension of the Standard Model*, JHEP **04** (2019) 052 [arXiv:1812.09333] [INSPIRE].

[44] G. Kurup and M. Perelstein, *Dynamics of Electroweak Phase Transition In Singlet-Scalar Extension of the Standard Model*, Phys. Rev. D **96** (2017) 015036 [arXiv:1704.03381] [INSPIRE].

[45] C.-Y. Chen, J. Kozaczuk and I.M. Lewis, *Non-resonant Collider Signatures of a Singlet-Driven Electroweak Phase Transition*, JHEP **08** (2017) 096 [arXiv:1704.05844] [INSPIRE].

[46] C.-Y. Chen, S. Dawson and I.M. Lewis, *Exploring resonant di-Higgs boson production in the Higgs singlet model*, Phys. Rev. D **91** (2015) 035015 [arXiv:1410.5488] [INSPIRE].

[47] A. Katz and M. Perelstein, *Higgs Couplings and Electroweak Phase Transition*, JHEP **07** (2014) 108 [arXiv:1401.1827] [INSPIRE].

JHEP12(2023)018

[48] P.H. Damgaard, A. Haarr, D. O'Connell and A. Tranberg, *Effective Field Theory and Electroweak Baryogenesis in the Singlet-Extended Standard Model*, *JHEP* **02** (2016) 107 [arXiv:1512.01963] [INSPIRE].

[49] P. Huang, A. Joglekar, B. Li and C.E.M. Wagner, *Probing the Electroweak Phase Transition at the LHC*, *Phys. Rev. D* **93** (2016) 055049 [arXiv:1512.00068] [INSPIRE].

[50] D. Curtin, P. Meade and C.-T. Yu, *Testing Electroweak Baryogenesis with Future Colliders*, *JHEP* **11** (2014) 127 [arXiv:1409.0005] [INSPIRE].

[51] J.M. No and M. Ramsey-Musolf, *Probing the Higgs Portal at the LHC Through Resonant di-Higgs Production*, *Phys. Rev. D* **89** (2014) 095031 [arXiv:1310.6035] [INSPIRE].

[52] W. Huang, J. Shu and Y. Zhang, *On the Higgs Fit and Electroweak Phase Transition*, *JHEP* **03** (2013) 164 [arXiv:1210.0906] [INSPIRE].

[53] P.H. Damgaard, D. O'Connell, T.C. Petersen and A. Tranberg, *Constraints on New Physics from Baryogenesis and Large Hadron Collider Data*, *Phys. Rev. Lett.* **111** (2013) 221804 [arXiv:1305.4362] [INSPIRE].

[54] A. Ashoorioon and T. Konstandin, *Strong electroweak phase transitions without collider traces*, *JHEP* **07** (2009) 086 [arXiv:0904.0353] [INSPIRE].

[55] S. Blasi and A. Mariotti, *Domain Walls Seeding the Electroweak Phase Transition*, *Phys. Rev. Lett.* **129** (2022) 261303 [arXiv:2203.16450] [INSPIRE].

[56] P. Ghorbani, *Vacuum structure and electroweak phase transition in singlet scalar dark matter*, *Phys. Dark Univ.* **33** (2021) 100861 [arXiv:2010.15708] [INSPIRE].

[57] K. Ghorbani and P.H. Ghorbani, *Strongly First-Order Phase Transition in Real Singlet Scalar Dark Matter Model*, *J. Phys. G* **47** (2020) 015201 [arXiv:1804.05798] [INSPIRE].

[58] A. Noble and M. Perelstein, *Higgs self-coupling as a probe of electroweak phase transition*, *Phys. Rev. D* **78** (2008) 063518 [arXiv:0711.3018] [INSPIRE].

[59] J.R. Espinosa and M. Quiros, *Novel Effects in Electroweak Breaking from a Hidden Sector*, *Phys. Rev. D* **76** (2007) 076004 [hep-ph/0701145] [INSPIRE].

[60] J.M. Cline and K. Kainulainen, *Electroweak baryogenesis and dark matter from a singlet Higgs*, *JCAP* **01** (2013) 012 [arXiv:1210.4196] [INSPIRE].

[61] S. Profumo, M.J. Ramsey-Musolf, C.L. Wainwright and P. Winslow, *Singlet-catalyzed electroweak phase transitions and precision Higgs boson studies*, *Phys. Rev. D* **91** (2015) 035018 [arXiv:1407.5342] [INSPIRE].

[62] Particle Data Group collaboration, *Review of Particle Physics*, *PTEP* **2022** (2022) 083C01 [INSPIRE].

[63] C.L. Wainwright, *CosmoTransitions: Computing Cosmological Phase Transition Temperatures and Bubble Profiles with Multiple Fields*, *Comput. Phys. Commun.* **183** (2012) 2006 [arXiv:1109.4189] [INSPIRE].

[64] R.N. Lerner and J. McDonald, *Gauge singlet scalar as inflaton and thermal relic dark matter*, *Phys. Rev. D* **80** (2009) 123507 [arXiv:0909.0520] [INSPIRE].

[65] H.-L. Li, M. Ramsey-Musolf and S. Willocq, *Probing a scalar singlet-catalyzed electroweak phase transition with resonant di-Higgs boson production in the 4b channel*, *Phys. Rev. D* **100** (2019) 075035 [arXiv:1906.05289] [INSPIRE].

JHEP12(2023)018

[66] ATLAS collaboration, *Measurement of the W-boson mass in pp collisions at $\sqrt{s} = 7$ TeV with the ATLAS detector*, Eur. Phys. J. C **78** (2018) 110 [*Erratum ibid.* **78** (2018) 898] [arXiv:1701.07240] [INSPIRE].

[67] ATLAS collaboration, *A detailed map of Higgs boson interactions by the ATLAS experiment ten years after the discovery*, Nature **607** (2022) 52 [*Erratum ibid.* **612** (2022) E24] [arXiv:2207.00092] [INSPIRE].

[68] CMS collaboration, *Combined Higgs boson production and decay measurements with up to 137 fb^{-1} of proton-proton collision data at $\sqrt{s} = 13$ TeV*, CMS-PAS-HIG-19-005 (2019).

[69] M. Cepeda et al., *Report from Working Group 2: Higgs Physics at the HL-LHC and HE-LHC*, CERN Yellow Rep. Monogr. **7** (2019) 221 [arXiv:1902.00134] [INSPIRE].

[70] L. Heinrich,, M. Feickert, and G. Stark,, *scikit-hep/pyhf: v0.7.5*, DOI:10.5281/ZENODO.1169739.

[71] L. Heinrich, M. Feickert, G. Stark and K. Cranmer, *pyhf: pure-Python implementation of HistFactory statistical models*, J. Open Source Softw. **6** (2021) 2823 [INSPIRE].

[72] L. Sartore and I. Schienbein, *PyR@TE 3*, Comput. Phys. Commun. **261** (2021) 107819 [arXiv:2007.12700] [INSPIRE].

[73] I. Schienbein, F. Staub, T. Steudtner and K. Svirina, *Revisiting RGEs for general gauge theories*, Nucl. Phys. B **939** (2019) 1 [*Erratum ibid.* **966** (2021) 115339] [arXiv:1809.06797] [INSPIRE].

[74] M.-X. Luo, H.-W. Wang and Y. Xiao, *Two loop renormalization group equations in general gauge field theories*, Phys. Rev. D **67** (2003) 065019 [hep-ph/0211440] [INSPIRE].

[75] M.-X. Luo and Y. Xiao, *Two loop renormalization group equations in the standard model*, Phys. Rev. Lett. **90** (2003) 011601 [hep-ph/0207271] [INSPIRE].

[76] M. Gonderinger, Y. Li, H. Patel and M.J. Ramsey-Musolf, *Vacuum Stability, Perturbativity, and Scalar Singlet Dark Matter*, JHEP **01** (2010) 053 [arXiv:0910.3167] [INSPIRE].

[77] B.A. Kniehl, A.F. Pikelner and O.L. Veretin, *mr: a C++ library for the matching and running of the Standard Model parameters*, Comput. Phys. Commun. **206** (2016) 84 [arXiv:1601.08143] [INSPIRE].

[78] J. Alwall et al., *MadGraph 5: Going Beyond*, JHEP **06** (2011) 128 [arXiv:1106.0522] [INSPIRE].

[79] T. Sjostrand, S. Mrenna and P.Z. Skands, *A Brief Introduction to PYTHIA 8.1*, Comput. Phys. Commun. **178** (2008) 852 [arXiv:0710.3820] [INSPIRE].

[80] DELPHES 3 collaboration, *DELPHES 3, A modular framework for fast simulation of a generic collider experiment*, JHEP **02** (2014) 057 [arXiv:1307.6346] [INSPIRE].

[81] M. Cacciari, G.P. Salam and G. Soyez, *The anti-k_t jet clustering algorithm*, JHEP **04** (2008) 063 [arXiv:0802.1189] [INSPIRE].

[82] CMS collaboration, *Identification of b-Quark Jets with the CMS Experiment*, 2013 JINST **8** P04013 [arXiv:1211.4462] [INSPIRE].

[83] M.E. Peskin and T. Takeuchi, *A New constraint on a strongly interacting Higgs sector*, Phys. Rev. Lett. **65** (1990) 964 [INSPIRE].

[84] M.E. Peskin and T. Takeuchi, *Estimation of oblique electroweak corrections*, Phys. Rev. D **46** (1992) 381 [INSPIRE].

JHEP12(2023)018

[85] GFITTER GROUP collaboration, *The global electroweak fit at NNLO and prospects for the LHC and ILC*, *Eur. Phys. J. C* **74** (2014) 3046 [arXiv:1407.3792] [INSPIRE].

[86] CDF collaboration, *High-precision measurement of the W boson mass with the CDF II detector*, *Science* **376** (2022) 170 [INSPIRE].

[87] J. de Blas, M. Pierini, L. Reina and L. Silvestrini, *Impact of the Recent Measurements of the Top-Quark and W-Boson Masses on Electroweak Precision Fits*, *Phys. Rev. Lett.* **129** (2022) 271801 [arXiv:2204.04204] [INSPIRE].

JHEP12(2023)018